Simulation of the Utah Forge 2022 hydraulic simulations

Sylvain Brisson, Brice Lecampion

July 2024

1 Introduction

The Utah FORGE project is an ongoing EGS test site located in the Basin and Range formation in Utah, United States, that aims at demonstrating the feasibility of harnessing the heat of hot but not naturally permeable deep crystalline rocks as well as de-risking this technology [Moore et al., 2019a]. The stimulation procedures are closer to what is usually found in the context of hydraulic fracturation for the oil and gas industry than what other previous EGS projects have done in the past with relying mostly on the so-called hydro-shearing technology. The test site is composed of two deviated wells with the goal to hydraulically connect their sub-horizontal sections by the creation of multiple hydraulic fractures filled with proppant material [Moore et al., 2023].

In this section we propose an analysis of hydraulic stimulation experiments performed within the Utah FORGE project in April 2022 using the mixed mode capabilities of the Pyfracx software developed within the EMOD project, along with scaling relationship coming from analytical solutions of tensile and shear ruptures due to fluid injections. Our analysis is restrained to axisymmetric simulations.

2 Description and data recorded during the hydraulic stimulations

2.1 Presentation of the Utah FORGE April 2022 stimulation experiment

Figure 1 shows the geometrical configuration of the April 2022 hydraulic stimulation experiment. At this time of the project, 4 deep wells had been drilled: the deviated well 16A in which the stimulation is performed and 3 vertical wells that were first drilled for rock properties and in-situ stress estimations that are used for seismic monitoring during the experiment. The stimulation has been performed in 3 different stages, each stimulating three different parts of the well but all around a depth of 2500 m TVD. These three stimulation stages have been made one after the other and isolated thanks to the use of bridge plugs. The stimulated well has been equipped before the stimulation with a steel casing, except for the last 40 m. The first stimulation stage has been performed in this terminating open-hole section. The two others have been performed behind the casing, after perforating holes in the later over a distance of 7 m.

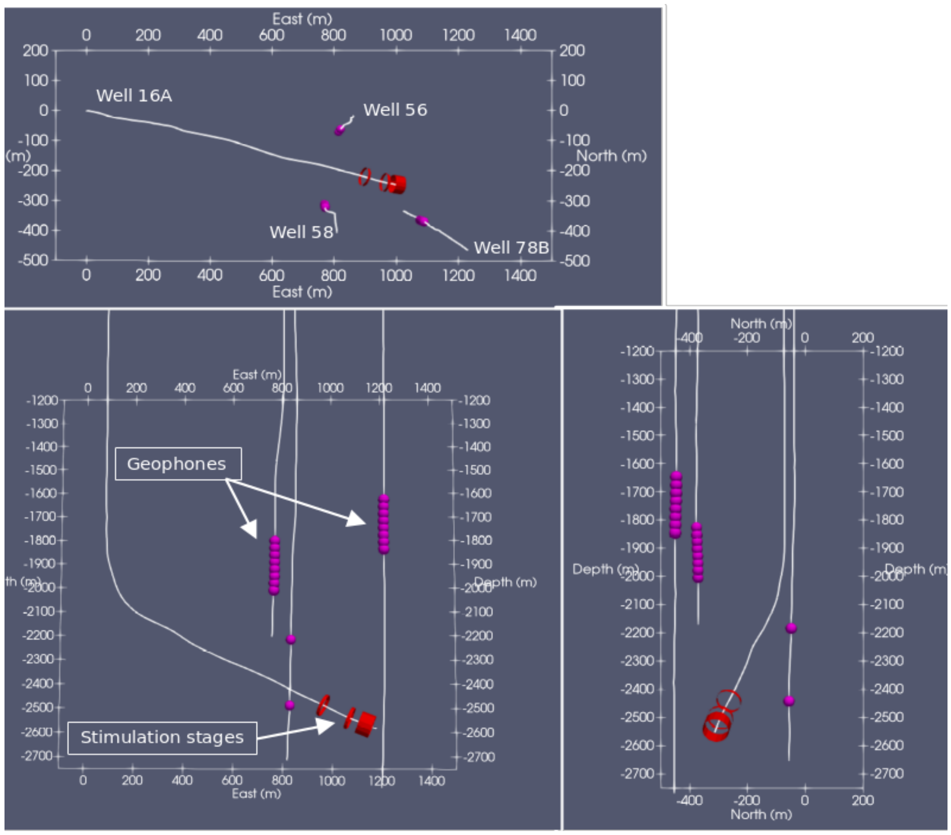

Figure 1: The April 2022 Utah FORGE hydraulic stimulation experiment: well, geophones and stimulated zones (top: view from top, bottom left: view from South, bottom right : view from East)

In this study, we restrict our analyses to the two stages that have been performed behind casing, excluding the first open-hole stage. These two stages differ primarily by the viscosity of the fluid used to perform the stimulation. In stage 2, slick water (water with additives aiming to reduce friction losses) has been used. The viscosity of the obtained fluid is of the same order of magnitude as water, around 10^{-3} Pa.s. It will be later referred to as the "slick-water" stage or as the stage 2. In stage 3, a polymer (cross-linked CMHPG polymer) has been added to water to get a more viscous fluid. As such it is referred as the "viscous fluid" stage. Its initial viscosity is measured to be around 1 Pa.s. However, at the high temperatures conditions encountered at the injection depth, the polymer is degraded over the time scale of the injection experiment leading to an important drop in the fluid viscosity, see Annex 6.1 for the results of the fluid viscosity evolution with time when exposed to the temperatures expected in the reservoir. Another key difference is that for stage 3, propant material (particles of size 1 to 200 μm used to fill tensile fractures and maintain its hydraulic conductivity on closure) has been pumped with the fracturing fluid. All details regarding how these hydraulic stimulations have been performed can be found in [Moore et al., 2023].

2.2 Rock properties and in-situ stress estimations

The elastic properties of the granitic rock in which the stimulation is performed have been estimated from core samples and are given as a Young elastic modulus around 60 GPa and a Poisson's ratio around 0.3 [Moore et al., 2019b].

Having a good estimation of the in-situ stresses of the reservoir where the stimulations are to be performed is critical to forecast the direction of propagation of hydraulic fractures or their characteristics. The stress state is modeled as 3 principal stresses constant and homogeneous vertical gradients, one being vertical and the two other horizontals. The vertical stress gradient $\partial_z \sigma_v$ is estimated from rock density profile integration (which is known thanks to well density logging). To get an estimation of the magnitude of the vertical gradients of the horizontal components σ_h and σ_H, the minimum and maximum horizontal stress gradients respectively, and their direction we rely on hydraulic stimulation experiments performed in the wells before casing. We settle for the in-situ stress model used in [Xing et al., 2022] and defined as :

$$\begin{aligned}
\partial_z \sigma_v &= 25\text{kPa/m} \\
\partial_z \sigma_H &= 19\text{kPa/m} \\
\partial_z \sigma_h &= 17\text{kPa/m} \\
\alpha_{\sigma_H} &= 25^\circ
\end{aligned}$$

Where α_{σ_H} is the azimuth (angle to the direction of the North) of the maximum horizontal stress direction. To correctly estimate the stress on the faults, we also need to estimate the pre-existing pore-pressure in the faults, supposing a porous material behavior. We settle for a hydro-static pore-pressure vertical profile, i.e. $\partial_z p = 9.8kPa/m$. At the depth of the stimulations, given these vertical gradient values, the in-situ stresses are $\sigma_v = 62.5$ MPa, $\sigma_H = 47.5$ MPa, $\sigma_h = 42.5$ MPa, and $p = 24.5$ MPa. We note that there are strong uncertainties on this stress state values and orientation. In this complex, fractured rock mass the real stress state is thought to be very heterogeneous [Mustafa et al., 2023]. This uncertainty is a major limiting factor to effectively model hydraulic stimulations knowing that these meter-scale stress heterogeneities drive the propagation of the aseismic rupture [Villiger et al., 2021]. Figure 2 shows the Mohr circles representation of this state of stress along with the Mohr-coulomb shear failure criterion for a friction coefficient of 0.6 and zero cohesion. This figure also represents the projected states of stress the closest to tensile failure and to shear failure.

The natural fractures present in this granitic rock have been modeled using the discrete fracture networks (DFN) approaches using data coming from imaging of the fractures crossed by the wells (with formation microresistivity imaging or FMI) as well as direct observations of the same formation where it is exposed to the surface. In [Aleta and Bryan, 2024], authors come to the model of a stochastic DFN composed of 4 fracture sets i.e. 4 main orientations of fractures. Figure 3 shows the orientation of these different fracture sets as well as the orientation of the observed fractures in the FMI log of the well 16A in the surrounding of the stimulation zones.

2.3 Injection rate and pressure data

The two stimulation stages have been performed following a similar injection rate schedule as shown in figures 4 and 5: a step-like increase to reach a plateau and then a step-like descent, both throughout 3 to 4 hours. Note that for stage 2 an arrest in the injection has been made

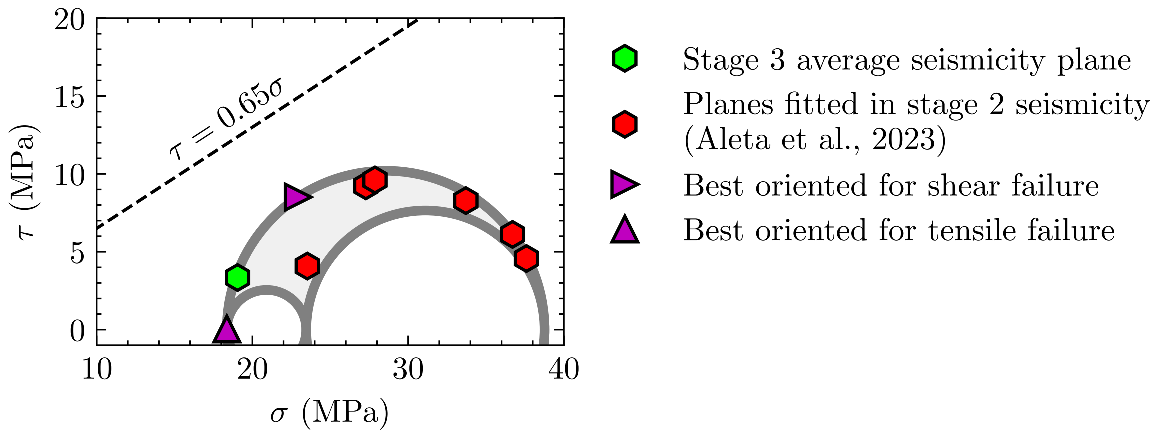

Figure 2: Mohr circles representation of the state of stress proposed by [Xing et al., 2022].

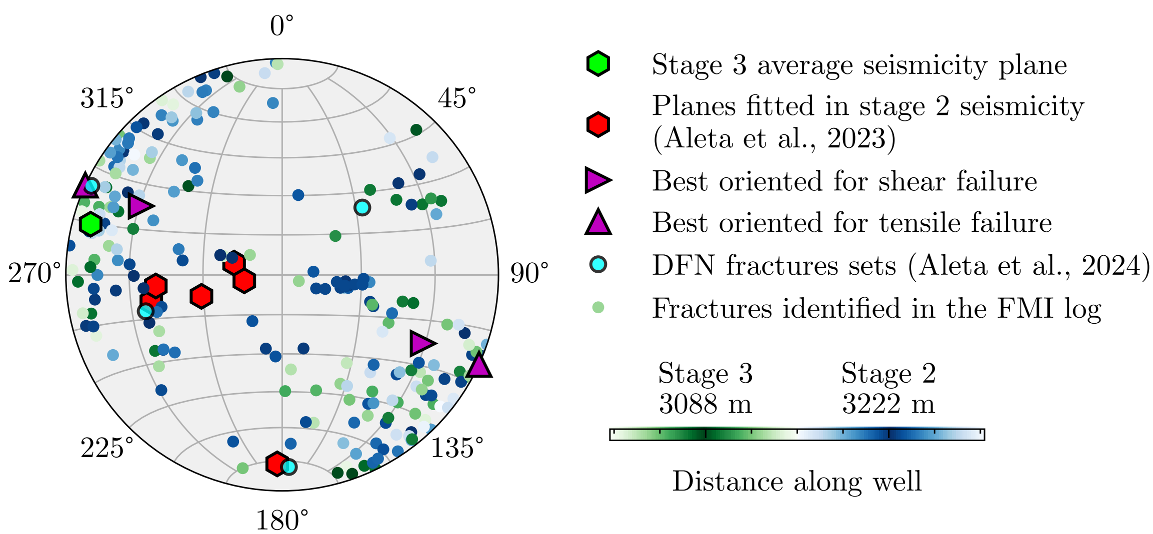

Figure 3: Stereonet representation of the different planes at stake: the fracture planes observed in the FMI log of well 16A in the vicinity of the stimulation zones, the mean orientation of the fractures set that compose the most up-to-date DFN model, the orientation of the planes used to project the seismic events to estimate the aseismic rupture area and the most favorable planes for tensile and shear rupture given the supposed stress state.

to study how the observable data, i.e. the pressure at the wellhead and the induced seismicity would behave in such a scenario. Note that in these figures the pressure is the one recorded at the well head, to get the pressure encountered in the well at the depth of the stimulations one must add the hydro-static part (around 25 MPa) and retrieve the pressure drop due to friction in the well (harder to estimate but below 10 MPa).

The injected volumes are similar for the two stages, around 400 m^3. The pressure responses are also similar. During the first 5 minutes we observe the pressurization of the well (the slope being the compressibility of the water content of the well also known as the wellbore storage

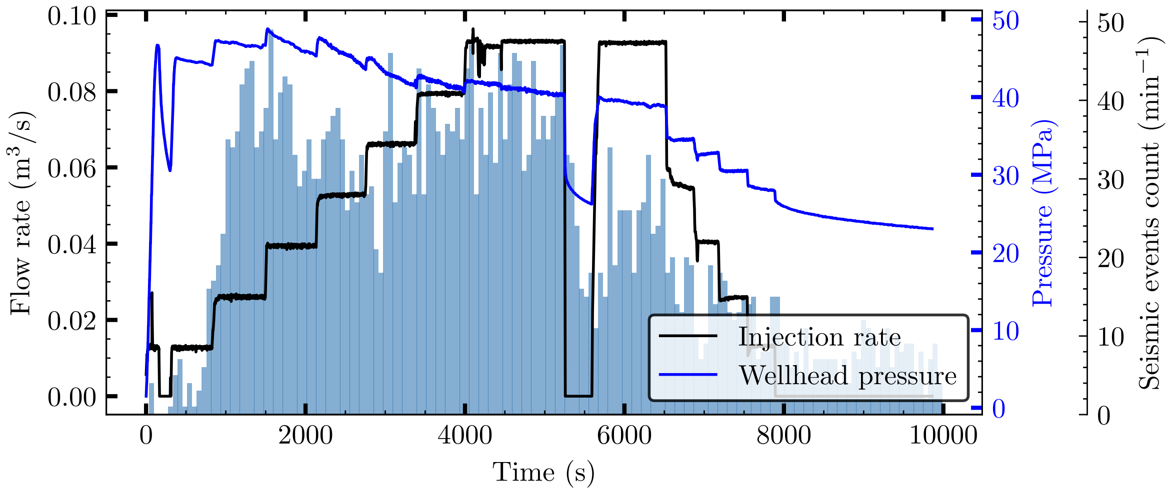

Figure 4: Stage 2 (slick water): injection flow rate and wellhead pressure

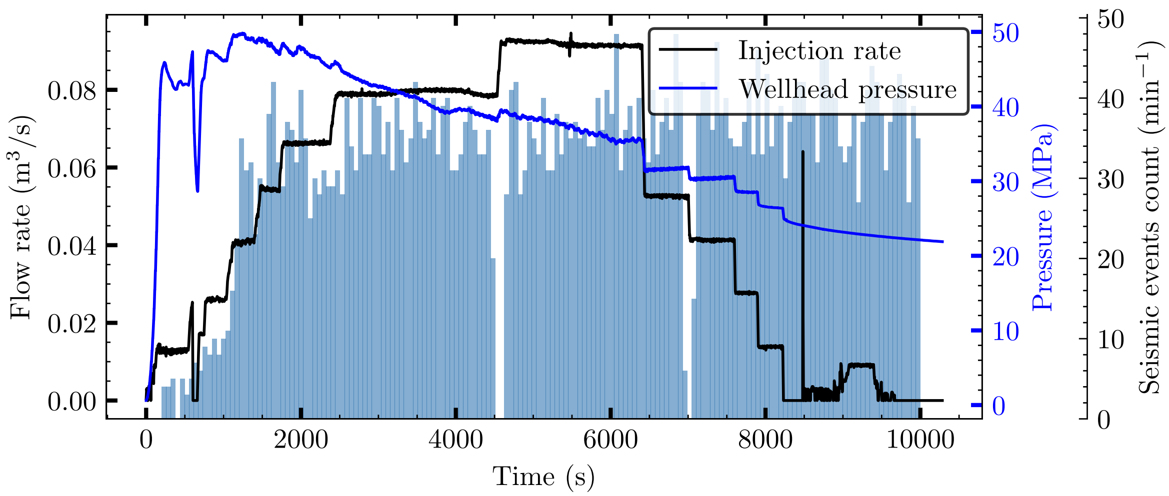

Figure 5: Stage 3 (viscous fluid): injection flow rate and wellhead pressure

coefficient). Then the breakout pressure is reached, between 40 MPa and 50 MPa for both stages. At this pressure, the stimulation begins: a fracture is opened or sheared which leads to a strong increase in its hydraulic conductivity and hence a well pressure decrease. Then for the rest of the stimulation we observe that despite the increasing injection rates the wellhead pressure keeps decreasing, indicating an efficient hydraulic stimulation of the reservoir.

2.4 Estimation of the evolution of the rupture surface from the located micro-seismicity catalog

As said in the introduction, even if hydraulic stimulation relies mostly on the development of aseismic ruptures, these come with the development of micro-seismic events due to small-scale heterogeneities of the stresses and/or the rock and faults material properties. In the absence of other geodetic measurements (such as tiltmeters), this induced seismicity is the only way of investigating how the stimulated reservoir has developed. We use the seismic catalog obtained by [Dyer et al., 2022]. The acceleration data used to get this catalog had been recorded by three-component geophones placed in deep wells close to the stimulation zone as represented on Figure 1. The number of recorded and located events for the two stages as well as the total seismic moments are reported in table 1. The seismic point clouds associated with the two studied stages are shown in Figure 6.

Table 1: Induced seismicity catalog

Stage	Number of recorded events	Total seismic moment	Maximum moment magnitude	Number of located events	Total seismic moment of located events	Mean location uncertainty
2 (slick water)	5456	3.5 10^{18} N.m	-0.23	1322	4 10^{17} N.m	58 m
3 (viscous fluid)	13135	9.3 10^{18} N.m	0.6	5283	4.1 10^{18} N.m	36 m

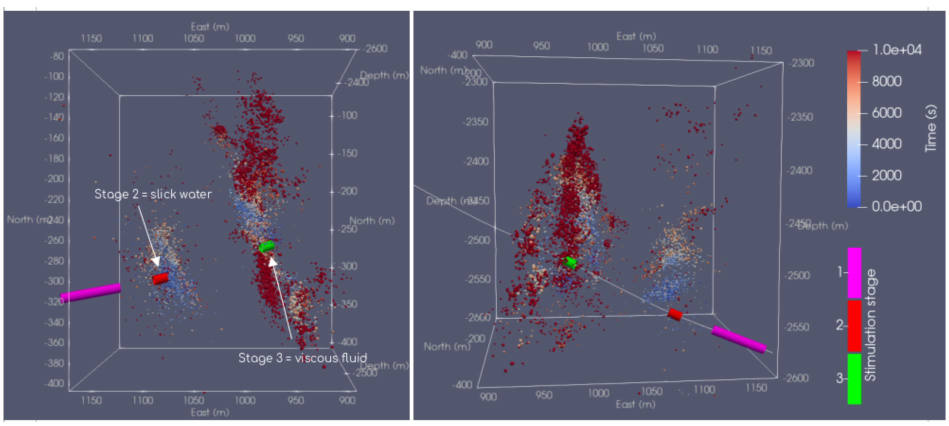

Figure 6: Induced seismicity catalog associated with the hydraulic stimulation, from [Dyer et al., 2022]. The events are represented as spheres whose radius depend on their magnitude and are colored by time starting from the start of injection of their respective stage.

We use the located events as a proxy of the shape and the size of the aseismic rupture. As can be seen in Figure 6 the acoustic emissions of the viscous fluid stage are, in the first order, distributed on a plane. Under the assumption that this rupture is indeed planar, we compute its area A and equivalent radius $R = \sqrt{A}/(2\pi)$ by computing the mean plane of the deformation through an SVD decomposition. We then project these events on the mean plane and we compute for given time steps t_i the convex hull of the projected events that have occurred before t_i. The area of these convex hulls is taken as the area of the aseismic rupture. For the slick-water stage, this procedure is complicated by the fact that the events point cloud cannot be reasonably taken as a plane. To estimate a rupture area we follow a similar procedure than for stage 3 but we use several planes rather than the mean seismicity plane. We project the events on the plane they are the closest to and sum up at each time the areas of the convex hulls constructed on each plane. The final results we obtain for both stages are shown in Figures 8 and 7. More details on the procedure of this analysis are given in Annex 6.2. We can see that, using this analysis, the equivalent rupture radius grows steadily for both stages to reach a radius of around 125 m for the viscous fluid stage and around 100 m for the slick water stage. We also observe that for the viscous fluid stage, the rupture seems to keep on propagating after the end of the injection. The uncertainty on the equivalent rupture radius for the 2nd stage is larger. It does not allow us to clearly state if propagation continues after the end of injection. No sensitivity analysis of these results has been performed varying the outliers determination parameters or the planes used for the multiple planes rupture area estimation. Note that the mean seismicity plane of stage 3 and the planes used for the surface area estimation of stage 2 orientations are represented in Figure 3. When we project the stress model on these planes as represented on Figure 2 we see that the mean seismicity plane of stage 3 is consistent with a tensile hydraulic fracture as its orientation is close to the preferred orientation for tensile fractures : normal to the minimal in-situ stress. On the other hand, some of the planes used for the surface estimation of stage 2 rupture could be geomechanically justified by being close to the preferred orientation for shear failure while others seem to not verify such mechanical justification given our state of stress model. Despite this we believe that the fracture surface estimation we get using these planes is better than the one we would get using only the mean seismicity plane as for stage 3: Figure 8 shows that by projecting on multiple planes we almost double the rupture equivalent radius.

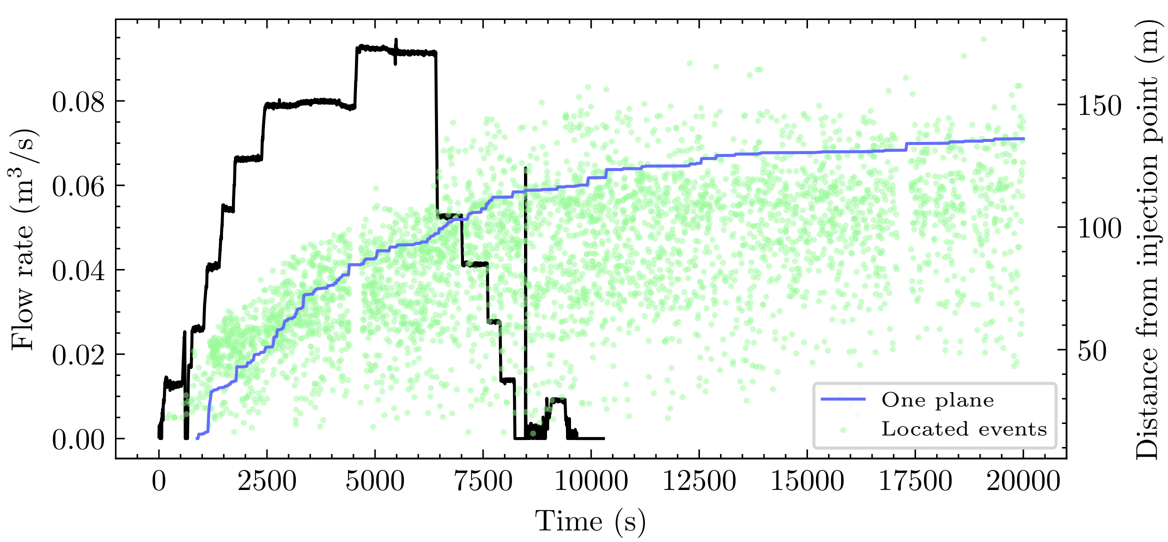

Figure 7: Stage 3 (viscous fluid): aseismic rupture surface estimation from the induced micro-seismicity

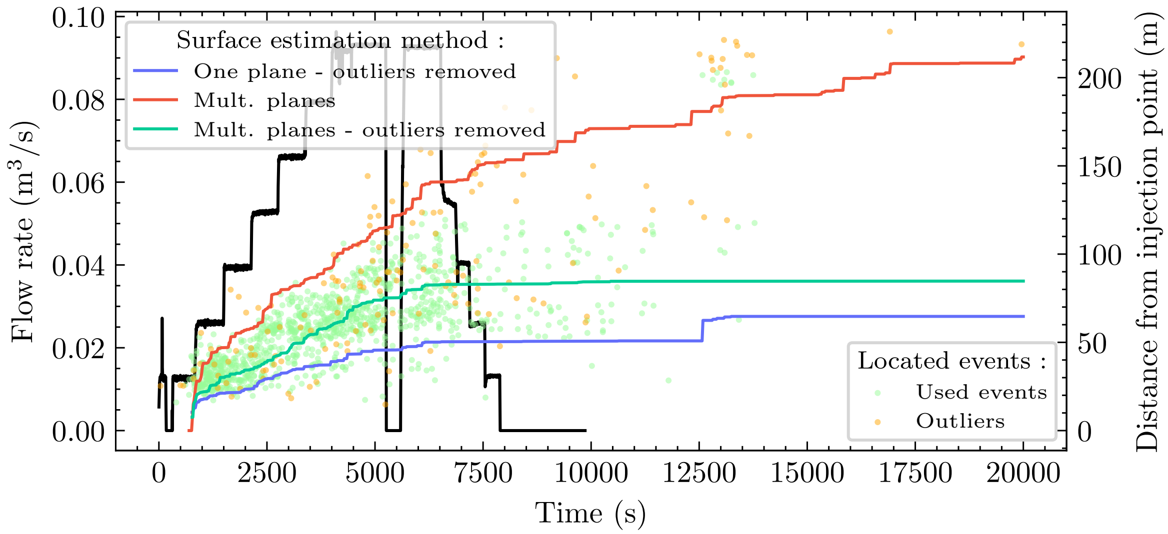

Figure 8: Stage 2 (slick water): aseismic rupture surface estimation from the induced micro-seismicity

3 Theoretical estimate of fluid-driven fractures propagation

Our analysis can be broken into two parts: a first part where we compare the observed relationship between rupture size and injected volume to scalings coming from fluid-driven shear rupture and hydraulic fracture analytical solutions and a second part where we use a fully coupled mixed-mode hydro-mechanical solver to perform simulations of the two hydraulic stimulation stages. The first part aims to help us understand the results of the second.

3.1 Analytical solution for the shear rupture (mode II) problem

For this, we rely on the results of [Sáez et al., 2022]. In the following we describe the problem the authors are interested in and its mathematical formulation. We suppose a fault plane Γ on the (x, y) plane that separates two semi-infinite isotropic homogeneous linear elastic solid and subject to a state of stress that projects as a normal component σ_0 and a shear component τ_0. This fault plane obeys a Coulomb friction yielding law with a constant friction coefficient and no cohesion. A fluid point source lying on the plane models the injection of a fluid from a wellbore crossing the interface. Finally, it is supposed that the rock is impermeable and that the fluid flows only within the fault interface with a constant permeability, independent of the mechanical deformation of the system. The hydro-mechanical problem is as such said to be uncoupled. The variables of the problem are the pore-pressure of the fluid along the fault plane $p(x, y, t)$ and the slip of the fault $\delta(x, y, t)$. The pore-pressure obeys equation 1 with S the storage coefficient (Pa^{-1}), a combination of the fluid compressibility and the porous interface material compressibility, k the hydraulic permeability (m^2) and η (Pa.s) the hydraulic dynamic viscosity. It is a diffusion equation with a constant hydraulic diffusion coefficient α (m^2/s) defined by $\alpha = k/\eta S$.

$$S\frac{\partial p}{\partial t} - \frac{k}{\eta}\nabla^2 p = 0 \tag{1}$$

With the appropriate boundary conditions corresponding to a line injection at a constant flow rate Q_0 in an infinite planar material of width w_h, one can solve 1 for the axisymmetric pore-pressure profile $p(r,t)$ which will be used as an input of the mechanical problem. This solution shows a characteristic pressure value of Δp^* defined as $\Delta p^* = Q_0\eta/4\pi k w_h$.The mechanical deformation problem, which variable is the fault slip δ is composed of two equations: the elastic equilibrium that relates the slip to the shear stress on the interface $\tau(x,y,z)$ through the boundary integral equation 2 and the interface failure criterion 3. Here μ is the shear elastic modulus, ν is the Poisson's ratio, and f the friction coefficient.

$$\tau(x,y,t) = \tau_0 + \int_\Gamma K(x-\xi, y-\zeta; \mu,\nu)\delta(\xi,\zeta,t)d\xi d\zeta \tag{2}$$

$$|\tau(x,y,t)| \leq f(\sigma_0 - p(r,t)) \tag{3}$$

Given this problem and its mathematical formulation, the authors show that for $\nu = 0$ the slip field becomes axisymmetric as well and obeys a self-similar behavior. They show that the rupture radius $R(t)$ follows the following equation :

$$R(t) = \lambda\sqrt{4\alpha t}$$

Where $\sqrt{4\alpha t}$ is a characteristic distance for the pore-pressure diffusion and λ is a constant parameter, a function of a unique non-dimensional parameter T referred to as the stress parameter :

$$T = \frac{f\sigma_0 - \tau_0}{f\Delta p*}$$

In the limit case of $\lambda \gg 1$, which is equivalent to $T \ll 1$ and referred to as the critically stressed case, the effect of the injection can be modeled as a point force, whose intensity can be obtained from the integration of eq. 1. In [Sáez Uribe, 2023, pp. 187–188] the authors obtain in this limit case the scaling relationship 4 that relates the shear rupture radius R_s to the injected volume V for arbitrary injection rate history.

$$R_s = \sqrt{\frac{2\alpha f\mu V}{(f\sigma_0 - \tau_0)4\pi k w_h}} \tag{4}$$

3.2 Analytical solution for the hydraulic fracture (mode I) problem

Here we make use of the work of [Adachi and Detournay, 2002] and [Garagash and Detournay, 2005]. This problem differs from the one defined previously by the fact that our interface plane is here only subjected to a normal stress σ_0 without any shear stress, we also suppose that the fluid can only flow within the opened fracture, and not within a porous material that would fill a pre-existing interface. The authors show that this problem is axisymmetric and that the two variables, the pressure profile $p(r,t)$ and the opening profile $w(r,t)$ follow similar equations than for the fault problem. This time, however, the flow and the mechanical problem are coupled: the hydraulic conductivity of the fracture depends on its opening. This new system of equations is hence composed of the elastic equilibrium, a boundary integral equation similar to 2 but function of the normal stress $\sigma(r,t)$ and the opening $w(r,t)$, the non-linear Reynolds diffusion equation 5 (that comes from the lubrication approximation) and the fracture energy equilibrium equation 6 which states that on the rupture front r_c the mode I stress intensity factor K_I must equal the toughness of the rock K_{Ic}.

$$\frac{\partial w}{\partial t} = \frac{1}{12\eta}\nabla.(w^3\nabla p) \tag{5}$$

$$K_I(r_c,t) = K_{Ic} \tag{6}$$

For this problem, the authors show that the fracture propagation can progress in two different regimes depending on how the energy is dissipated: the system can dissipate energy mostly through flow friction: the viscosity-dominated regime (denoted as the M-solution) or through fracture surface creation: the toughness-dominated regime (denoted as the K-solution). It is shown that, given the material properties values usually encountered in the case of hydraulic fracturation of rock masses, the rupture propagation is likely to first transition from an initial propagation stage to the viscosity-dominated regime around the first characteristic time t_{om} and then transition from this viscosity-dominated regime to a toughness-dominated regime around a second characteristic time t_{mk}. Noting $E' = E/(1-\nu^2)$, $\eta' = 12\eta$ and $K' = 4\sqrt{2/\pi}K_{Ic}$, these two times take the following expression :

$$t_{om} = \frac{E'^2\eta'}{\sigma_0^3} \tag{7}$$

$$t_{mk} = \sqrt{\frac{E'^{13}\eta'^5 Q_0^3}{K'^{18}}} \tag{8}$$

For the two limit regimes the following scaling relationships are given (m standing for the viscosity-dominated regime and k for the toughness-dominated regime) to relate the hydraulic fracture radius to the volume of injected fluid V :

$$R_m \simeq 0.7\left(\frac{E'V^3t}{\eta'}\right)^{1/9} \tag{9}$$

$$R_k \simeq 0.85\left(\frac{E'^2V^2}{K'^2}\right)^{1/5} \tag{10}$$

3.3 Fully coupled hydro-mechanical mix-mode numerical solver

To simulate the studied hydraulic stimulation stages, we need to solve the full coupled hydro-mechanical problem, accounting for shear and tensile failure of fractures and the associated hydraulic permeability enhancements as well as variable injection flow rates. The developed model is similar to the single-failure models we have already introduced: we have to solve for a pore-pressure field $p(\boldsymbol{x},t)$ and an interface displacement discontinuity field $\boldsymbol{u}(\boldsymbol{x},t)$ with $\boldsymbol{x} \in \Gamma$, Γ being a set of preexisting interfaces. The displacement discontinuity is a vectorial quantity of the deformation at the surface of the fracture. It is important to note that in this model we take the fracture planes Γ as an apriori and we do not solve for the fractures geometry. These two fields must obey a system of 3 equations: the elastic equilibrium, which relates the stresses to the displacement knowing the elastic properties of the rock, the fluid flow equation, and the interface constitutive equation. The elastic equilibrium equation is again a boundary integral equation, similar to 2 but this time being vectorial, relating the traction vector to the displacement discontinuity vector. The fluid flow equation models the flow within a porous material of constant storage S (the sum of the fluid compressibility and the porous material compressibility) but variable width w and variable permeability k which is expressed as 11. The width is defined as $w = w_0 + u_n$, w_0 being the initial hydraulic width of the fault plane and u_n the normal opening of the interface. The permeability, under the lubrication approximation as in the hydraulic fracture model, follows equation 12.

$$S\frac{\partial wp}{\partial t} = \nabla.\left(\frac{wk(u_n)}{\eta}\nabla p\right) \tag{11}$$

$$wk(u_n) = \frac{(w_0 + u_n)^3}{12} \tag{12}$$

The third element of this model is the interface constitutive relation, which relates the effective traction $\boldsymbol{T'} = \boldsymbol{T} + p\boldsymbol{n}$ ($\boldsymbol{T}$ being the total traction, p the pore-pressure, and $\boldsymbol{n}$ a normal unit vector to the fracture surface) to the displacement discontinuity $\boldsymbol{u}$. We use an elasto-plastic constitutive relation that first deforms elastically, given shear and normal interface stiffness parameters, until a failure criteria is reached on which the interface starts to deform in an inelastic (referred as plastic) manner. In this regards the displacement discontinuity is decomposed in an elastic and a plastic part : $\boldsymbol{u} = \boldsymbol{u}^e + \boldsymbol{u}^p$. Two failure criterion are introduced, one for shear failure (mode II) F_{shear} and one for tensile failure (mode I) F_{tensile}, each of them is associated with a plastic flow rule to compute the inelastic displacements when a failure criterion is reached in a way to ensure that the tractions remain on the yielding surface. The parameters that define these failure criteria and the plastic flow rules depend on internal variables to be able to account for the damage of the interface : a shear damage variable χ_s and a total damage variable χ_t that are defined respectively as the maximum of the shear part and the norm of the encountered inelastic displacements. The shear failure criterion is the Mohr-Coulomb criterion but with changing friction coefficient as defined in 13 where $\boldsymbol{\tau}$ is the shear component of $\boldsymbol{T'}$ and T'_n is its normal component. In our model, the friction coefficient drops from an initial value f_p to a residual value $f_r < f_p$ over a slip weakening distance δ_c. The tensile failure criterion is defined as 14 where tensile failure is reached when the normal effective traction reaches the tensile strength of the material σ_t which is degraded to zero over a critical tensile weakening distance w_c.

$$F_{\text{shear}}(\boldsymbol{T'}, \boldsymbol{\chi}) = ||\boldsymbol{\tau}|| - f(\chi_s)T'_n \tag{13}$$

$$F_{\text{tensile}}(\boldsymbol{T'}, \boldsymbol{\chi}) = T'_n - \sigma_t(\chi_t) \tag{14}$$

Note that the degradation of the friction coefficient and the tensile strength with the inelastic displacement discontinuity define a shear and a tensile fracture energy. In the following use case, if not specified otherwise, we will set the tensile strength to zero which corresponds to zero tensile fracture energy i.e. zero tensile toughness.

To make this model complete we have to define how the interface deforms when the failure criteria are reached. For the tensile failure case, we use an associated plastic flow rule whereas for the shear failure case, we go for a non-associated plastic flow rule to account for dilatancy. This dilatancy defines that under shear failure, the interface shows normal opening as defined by 15. The dilatancy coefficient is chosen to drop from an initial value ψ_p to zero over the slip weakening distance.

$$\dot{u}_n = \psi(\chi_s)||\dot{\boldsymbol{\delta}}|| \tag{15}$$

To summarize, our model solves for the coupled problem of the fluid flow from an injection point within a set of fracture planes and the deformation of these same fracture planes. In one way the coupling lies in the fact that the fluid pore-pressure alters the initial stress condition of the fracture, while on the other way, it is in how the fault inelastic normal opening, that can be caused by tensile failure or by dilatant shear failure, change the fault permeability.

For what it is of the numerical implementation, we discretize our geometry into a mesh and then rely on a boundary element formulation of the rock elastic equilibrium problem and a finite element formulation of the fluid diffusion problem. The interface constitutive equation is a local equation and it is integrated at every node of the mesh at each solver's iteration. The problem is highly non-linear, due to the cubic dependence of the permeability on the fracture opening, we rely on a fully implicit solver for the time-stepping and use a Newton-Raphson algorithm at each time-step to solve the coupled hydromechanical systems. The model parameters are :

- The initial in-situ stresses before fluid injection σ_{ij}
- The elastic properties of the rock, ex: the Young's elastic modulus E and the Poisson's ratio ν
- The hydraulic properties of the interface: its storage S (which is usually taken as the compressibility of water) and its initial hydraulic width w_0
- The fluid dynamic viscosity η
- The interface constitutive equation parameters: its stiffnesses k_s and k_n (for shear and normal elastic deformation), the shear failure parameters (f_p, f_r, ψ_p, and δ_c) and the tensile failure parameters (σ_t and w_c)

4 Results

4.1 Comparison to scalings coming from analytical solutions

We first analyze the two stages as if they were hydraulic fractures. For that, we compute the transition times t_{om} and t_{mk} given by 7 and 8. The values of the various parameters are given in Table 2. With these values, we found that the first transition time t_{om} is very small compared to the total stimulation time which is around 10^4 s : 0.1 s and 10^{-3} s for the viscous fluid and the slick water viscosity values respectively. This indicates that for both viscosities a hydraulic fracture would have at least transitioned to the first viscosity-dominated regime. We then compute the second transition time t_{mk} to see if such hydraulic fractures would have transitioned in the second toughness-dominated regime or remained in the first viscosity-dominated regime. For the viscous fluid stage, we find a value of 4.10^6 s, this being much greater than the injection time, a hydraulic fracture would have remained in the viscosity-dominated regime. For the slick water stage, however, we find a value of 10 s that indicated that in these conditions a hydraulic fracture would have mostly developed in the toughness-dominated regime.

Table 2: Material properties and parameters used for the rupture radius - injected volume scaling analysis

Young's modulus E	60 GPa
Poisson's ratio ν	0.3
Mode I toughness K_{Ic}	2.5 MPa/m$^{1/2}$
Mean injection rate Q_0	0.05 m^3/s
Normal stress σ_0	30 MPa
Viscosity η (slick-water)	8.10^{-4} Pa.s
Viscosity η (viscous fluid)	0.1 Pa.s

Now supposing that the observed ruptures are critically stressed shear ruptures, we compute the expected pressure increase that would be associated with such a rupture. To do that, we need to suppose a fault initial transmissibility $[kw_h]_0$, we go for the value of 10^{-14} m^3 which is not properly estimated from pre-stimulation test of the stimulated zone but taken from literature of other test site studies [Ortiz R et al., 2011]. Then supposing that the shearing is dilatant, with a dilatancy coefficient $\psi = 0.1$ going to zero over a slip distance $\delta_c = 5$ mm, the shearing of the fault over a slip distance greater than δ_c would increase this fault zone permeability to the value $[kw_h]_f = [kw_h]_0 + (\psi\delta_c/2)^3/12 \simeq 10^{-12}$ m^3. Given these values of transmissibility, we can compute the associated expected pressure increases Δp^* which are summarized in Table 3. This simple calculation shows that, given reasonable transmissibility values, a shear rupture is not sufficient is the case of the high viscosity of the fluid used in stage 3 : the pressure increase being way larger than the minimum in-situ stress. For the slick-water stage, however, we see that given reasonable values of transmissibility increase trough dilation, the characteristic injection pressure could remain below the in-situ minimum stress and, hence an aseismic shear rupture associated with dilation could explain the observed stimulation.

We compare for both stages the observed relationship between the rupture radius and the injected volume to the scaling relationships expected for a hydraulic fracture, in the propagation regime found previously, and to the scaling expected for a critically stressed shear rupture. These results are shown on Figures 10 and 9. We observe that the stage 3 observation scales well with expected scaling relationship (the viscosity-dominated hydraulic fracture) and that the stage 2, which rupture equivalent radius is subject to greater uncertainty, does follow both the scalings of the toughness-dominated hydraulic fracture and of the critically stressed shear rupture. Note that given the accuracy of our estimation of the aseismic rupture area from the micro-seismicity catalog, it is impossible to tell if a scaling of the rupture radius

Table 3: Characteristic injection pressures $\Delta p^* = Q_0\eta/4\pi k w_h$ supposing only shear-induced dilation

	$[kw_h]_0 = 10^{-14}$ m^3	$[kw_h]_f = 10^{-12}$ m^3
Slick water: $\eta = 8.10^{-4}$ Pa.s	300 MPa	2.5 MPa
Viscous fluid: $\eta = 0.1$ Pa.s	40 GPa	300 MPa

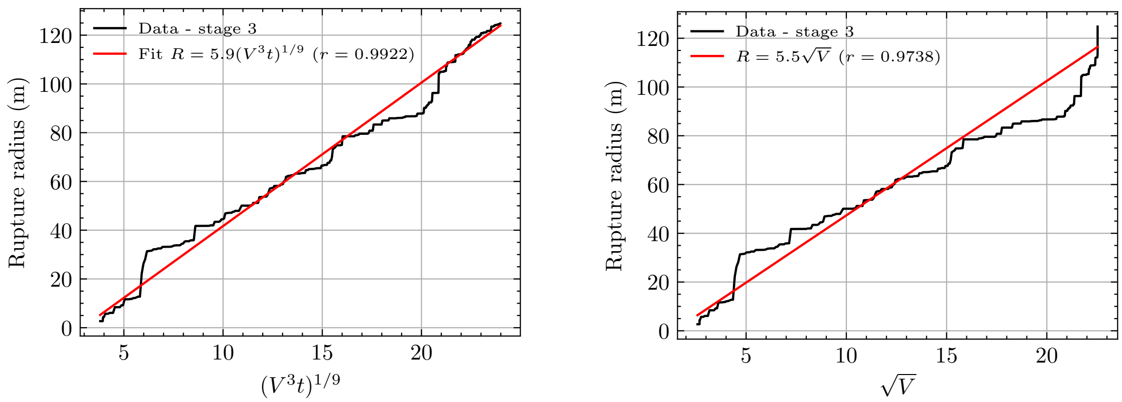

(a) Hydraulic fracture, viscosity-dominated scaling

(b) Critically stressed shear rupture scaling

Figure 9: Stage 3 (viscous fluid): comparison of the observed rupture radius - injected volume relation to hydraulic fracture and shear rupture scalings

to the injected volume with an exponent of 0.5 (shear rupture) fits the data better than an exponent of 4/9 (hydraulic fracture).

4.2 Simulation of the stimulations using a mixed-mode fully coupled hydro-mechanical solver

The use of analytical solutions as tools to discriminate between shear and tensile rupture has shown us that the viscous fluid stage is very likely a viscosity-dominated hydraulic fracture while the slick-water stage could be a shear rupture, a toughness-dominated hydraulic fracture or a mix of both. We confirm such observations by using the model described in section 3.3 to perform simulations modeling these two stages.

For both stages, we use the same parameter values as defined in Table 4. Simulations are performed on a single fault plane supposing an axisymmetric problem using a 1D mesh of size 500 m and a mesh size of 0.5 m. The one-fault axisymmetric approximation allows to greatly reduce the numerical cost of the simulation. We know that the axisymmetric approximation, which make us setting the Poisson's ratio value to zero, only affect the shape of the shear rupture that is modeled taken as circular while it should be elliptical for a non-zero Poisson's ratio [Sáez et al., 2022]. The one-fault approximation appears justified for stage 3 where

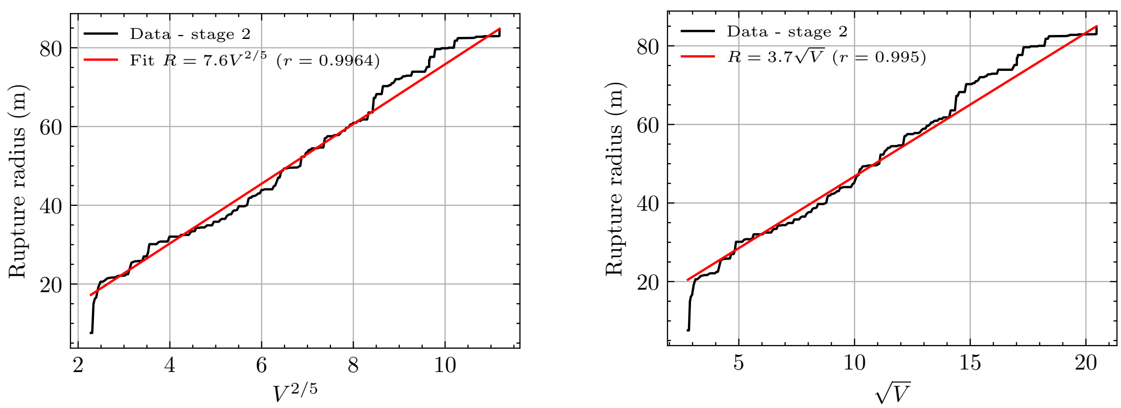

(a) Hydraulic fracture, toughness-dominated scaling

(b) Critically stressed shear rupture scaling

Figure 10: Stage 2 (slick water): comparison of the observed rupture radius - injected volume relation to hydraulic fracture and shear rupture scalings

the induced seismicity appears to lie on a single plane. For stage 2, where we have seen that the rupture geometry is more complex and probably involves multiple planes, it is a stronger approximation. It can be justified for shear critically stressed rupture knowing it has been shown that a network of stress fault has a similar behavior that the one of a single fault [Ciardo and Lecampion, 2022]. For the in-situ state of stress, we try two end cases corresponding to the projection of the same state of stress previously defined but projected on two different planes: the T-plane, which is the most favorably oriented for tensile failure, and the S-plane, which is the most favorably oriented for shear failure. As it is shown on Figure 2. The normal and shear stress obtained after projection are indicated in Table 5. We hence end up performing 4 simulations, for the two possible values of stress and the two possible values of fluid viscosity.

Note that here, by taking σ_t the tensile strength of the fault plane constant equal to zero we neglect the mode I fracture energy. This is justified in the case of the viscous fluid stage as we are in the viscosity-dominated regime. For the slick-water stage, where we should be in the toughness-dominated regime for a hydraulic fracture propagation, this can be justified if the fault starts to shear enough such that it is fully broken before it starts to open. However this approximation is questionable in the case of the simulation of the same slick-water stage using the stresses projected on the T-plane where no shearing occurs.

The results of these 4 simulations are shown on Figures 14 and 13 for the slick water stage and on Figures 14 and 11 for the viscous fluid stage. For each stage we show the evolution with time of the pressure at the injection node, to be compared with the recorded wellhead pressure, and the rupture radius (that can be a shear or a tensile rupture), to be compared with the estimation from the induced micro-seismicity. We also show at a given time step at 4000 s after the start of the injection, how the pressure, slip, opening, and transmissibility profiles evolve with the distance to the injection point.

For the viscous fluid stage, we find back the expected results from section 4.1: when taking the closest possible state of stress to shear failure (S-plane) a shear fracture does develop

Table 4: Material properties and parameters used for the numerical simulations

Young's modulus $E^{(1)}$	60 GPa
Poisson's ratio ν	0.0 (axisymmetric)
Fracture shear stiffness ${k_s}^{(2)}$	$50 * E = 300$ GPa
Fracture normal stiffness ${k_n}^{(2)}$	$50 * E = 300$ GPa
Peak friction coefficient ${f_p}^{(2)}$	0.65
Residual friction coefficient ${f_r}^{(2)}$	0.6
Peak dilatancy coefficient ${\psi_p}^{(2)}$	0.1
Slip weakening distance ${\delta_c}^{(2)}$	2.5 mm
Fracture hydraulic compressibility $S^{(3)}$	2.10^{-9} Pa^{-1}
Fracture initial transmissibility $[kw_h]_0$ $^{(2)}$	10^{-14} m^3
Wellbore storage $^{(4)}$	2.8 10^{-8} Pa^{-1}

[1] Estimated from rock core sample analysis
[2] Common values found in the literature for fractures in granitic rocks
[3] Value allowing us to match the shear rupture radius
[4] Estimated from well pressurization analysis

but the transmissibility increase due to the associated dilation is not enough to prevent the buildup of pressures high enough to lead to the development of a tensile fracture. This is shown in Figure 11. For both states of stress for this stage we observe the development of a hydraulic fracture, whose radius is coherent with the observations, and which allows for the considerable transmissibility increase that explains the continuous pressure decrease at the injection point despite the increasing injection rate.

For the slick water stage, however, we find that given our model parameters the modeled physics is very different depending on the state of stress we choose. As shown in Figure 13, when we project the stresses on the T-plane the stimulation is well represented by a hydraulic fracture while when projected on the S-plane the stimulation is well represented by a shear rupture with a normal opening only due to the associated dilatancy. We observe that both these possibilities lead to a rupture radius aligned with the one estimated from the micro-seismicity and to consistent pressure drop-out. Comparing the pressure simulated at the injection point to the recorded wellhead pressure in Figure 14, one could find that the hydro-shearing hypothesis could be a better fit for how the wellhead pressure reacts to the injection stop around 5500 s as well as to the rate step increase or decrease.

Note that by comparing directly the recorded wellhead pressures to the simulated pressure at the injection node we suppose that an initial pore-pressure is the hydro-static pressure and we neglect the pressure losses through friction in the well or at the entry thought the perforation of the casing. These friction pressure losses can be estimated, using the work of [Lecampion and Desroches, 2015], and are found to be between 1 and 10 MPa. Even using

Table 5: Shear and normal stress values

	Normal stress σ_0	Shear stress τ_0
T-plane (closest to tensile failure)	18.4 MPa	0.0 MPa
S-plane (closest to shear failure)	23 MPa	8.54 MPa

the upper estimation of 10 MPa of pressure losses due to friction, there remains a difference of 10 to 20 MPa between the simulated and the observed pressures. This gap could be explained by several factors such as errors in the in-situ stresses estimation or strong friction losses due to important fracture geometry tortuosity in the near-wellbore area.

5 Conclusions

In this study, we have compared and modeled two hydraulic stimulation stages differing only by the viscosity of the fluid used to perform the stimulation. After having estimated the area of the aseismic ruptures associated with these stimulation operations using the associated induced micro-seismicity, we have shown using parametric studies and scaling relationship coming from hydraulic fracture and shear rupture theory that the rupture induced by the more viscous fluid could only be a viscosity-dominated hydraulic fracture while the rupture associated with the less viscous fluid could be modeled by a toughness-dominated hydraulic fracture or by a critically stressed shear rupture and is likely a combination of both composed of multiple fracture planes. Finally, we have confirmed these results through axisymmetric simulations of these stimulations experiments that were able to effectively reproduce the observed aseismic rupture surfaces but did not reproduce the elevated observed pressures though to be caused by unmodelled friction physics and/or errors in in-situ stress estimations.

During this 4 months internship, I have spent my time on extremely varied tasks. I have dived into the modeling of the hydro-mechanical problems of injection-induced shear and tensile rock fractures and have spent time improving my understanding of the numerical methods used to come to a solver for such non-linear problems. My work has then consisted on one hand in getting the data from the Utah FORGE data repository and analyzing it and on the other hand in improving the solver and performing benchmarks and simulations. For the upcoming I would like to continue in this direction of physical and numerical modeling of these complex problems with varied applications, while adding an experimental component to my work.

References

[Adachi and Detournay, 2002] Adachi, J. I. and Detournay, E. (2002). Self-similar solution of a plane-strain fracture driven by a power-law fluid. *International Journal for Numerical and Analytical Methods in Geomechanics*, 26(6):579–604.

[Aleta and Bryan, 2024] Aleta, F. and Bryan, F. (2024). Updated reference discrete fracture network model at utah forge. *Stanford Geothermal Workshop*.

[Aleta et al., 2023] Aleta, F., Bryan, F., and Podgorney, R. (2023). Development of a discrete fracture network model for utah forge using microseismic data collected during stimulation of well 16a(78)-32. *Stanford Geothermal Workshop*.

[Ciardo and Lecampion, 2022] Ciardo, F. and Lecampion, B. (2022). Injection-induced aseismic slip in tight fractured rocks. Technical report. arXiv:2212.01050 [physics] type: article.

[Dyer et al., 2022] Dyer, B., Karvounis, D., and Bethmann, F. (2022). Utah forge: Updated seismic event catalogue from the april, 2022 stimulation of well 16a(78)-32.

[Garagash and Detournay, 2005] Garagash, D. I. and Detournay, E. (2005). Plane-Strain Propagation of a Fluid-Driven Fracture: Small Toughness Solution. *Journal of Applied Mechanics*, 72(6):916–928.

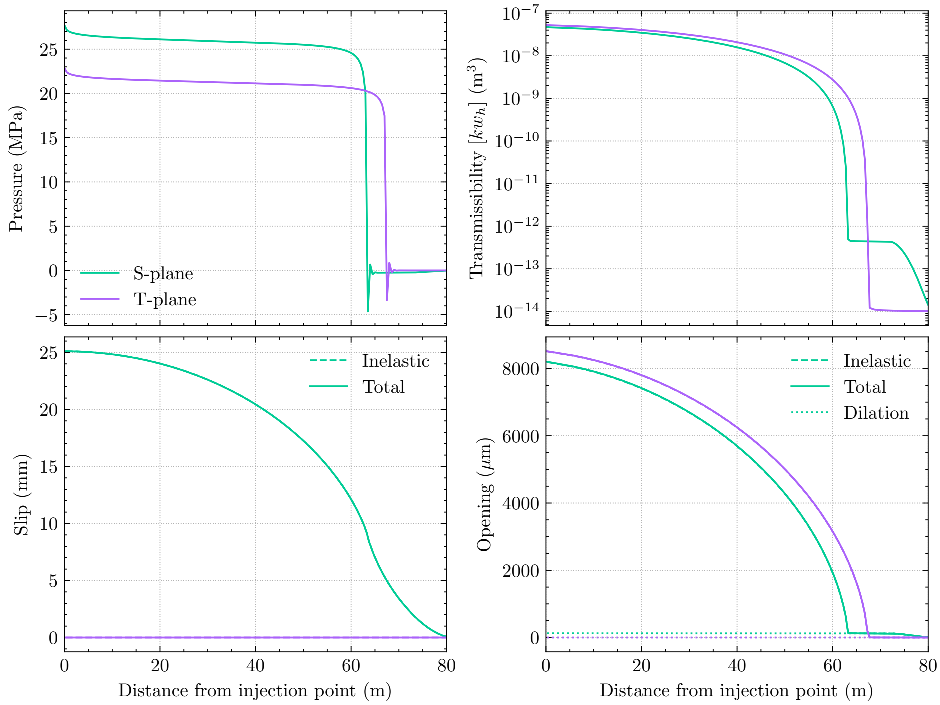

Figure 11: Simulation of stage 3 (viscous fluid): profiles of fluid pore pressure, slip, opening and hydraulic transmissibility

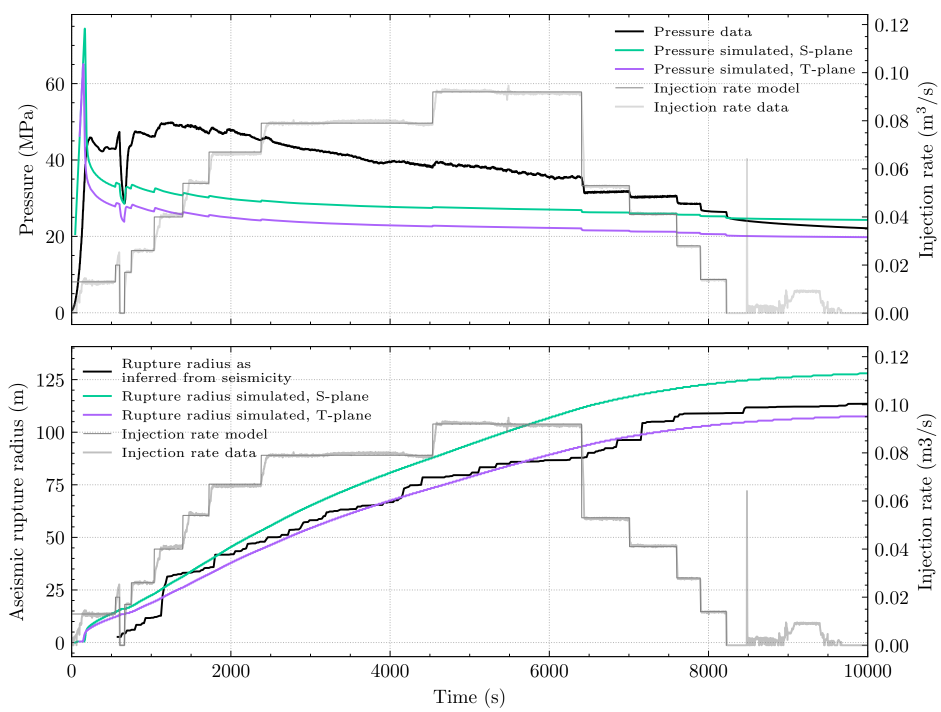

Figure 12: Simulation of stage 3 (viscous fluid): pore pressure record at the injection point and rupture radius.

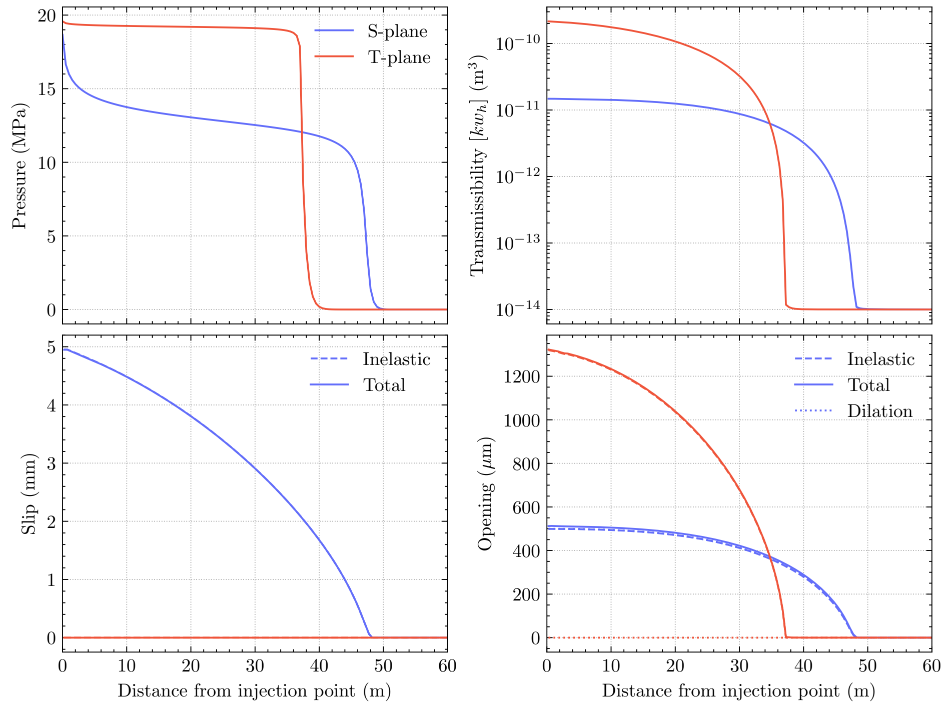

Figure 13: Simulation of stage 2 (slick water): profiles of fluid pore pressure, slip, opening and hydraulic transmissibility

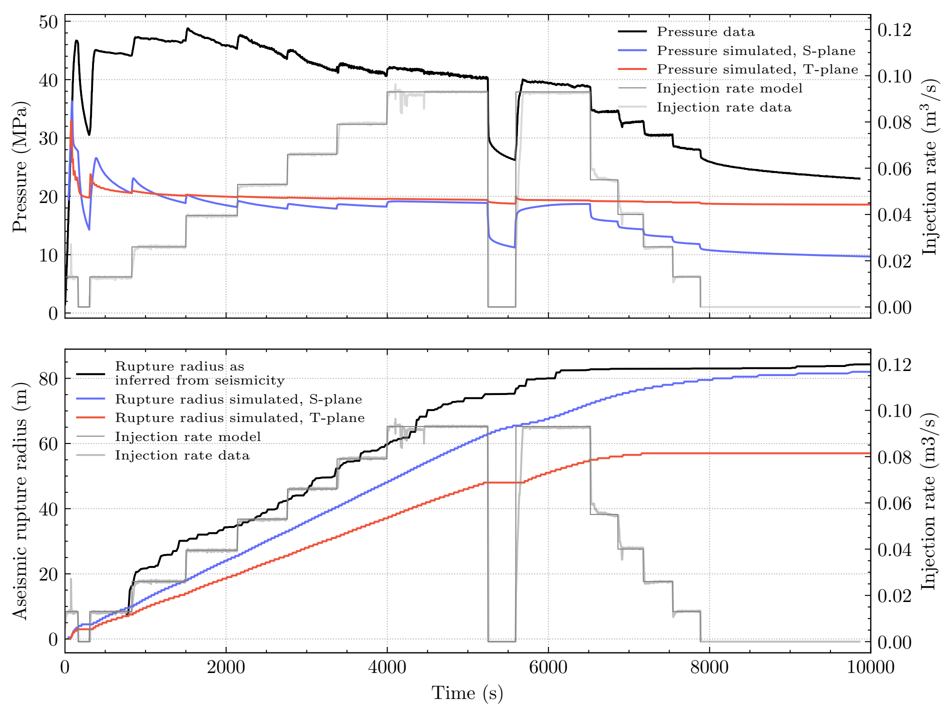

Figure 14: Simulation of stage 2 (slick water): pore pressure record at the injection point and rupture radius.

[Lecampion and Desroches, 2015] Lecampion, B. and Desroches, J. (2015). Simultaneous initiation and growth of multiple radial hydraulic fractures from a horizontal wellbore. *Journal of the Mechanics and Physics of Solids*, 82:235–258.

[Moore et al., 2019a] Moore, J., McLennan, J., Allis, R., Pankow, K., Simmons, S., Podgorney, R., Wannamaker, P., Bartley, J., Jones, C., and Rickard, W. (2019a). The utah frontier observatory for research in geothermal energy (forge): an international laboratory for enhanced geothermal system technology development. In *44th Workshop on Geothermal Reservoir Engineering*, pages 11–13, Stanford, California. Stanford University.

[Moore et al., 2019b] Moore, J., Simmons, S., McLennan, J., Jones, C., Skowron, G., Wannamaker, P., Nash, G., Hardwick, C., Hurlbut, W., Allis, R., Kirby, S., Erickson, B., Feigl, K., Batzli, S., Miller, J., Witter, J., Podgorney, R., Pankow, K., Reinisch, E., Patel, V., Martin, T., Rutledge, J., and McKean, A. (2019b). Utah forge: Phase 2c topical report.

[Moore et al., 2023] Moore, J., Wannamaker, P., McLennen, J., Pankow, K., Skowron, G., Nash, G., Jones, C., Barker, B., Podgorney, R., and Simmons, S. (2023). Utah forge: 2023 phase 3b year 1 annual report.

[Mustafa et al., 2023] Mustafa, A., Bunger, A., and Kelley, M. (2023). Utah forge project 2439: Machine learning for well 16a(78)-32 stress predictions - september 2023 report. Technical report.

[Ortiz R et al., 2011] Ortiz R, A., Renner, J., and Jung, R. (2011). Hydromechanical analyses of the hydraulic stimulation of borehole basel 1. *Geophysical Journal International*, 185(3):1266–1287.

[Sáez et al., 2022] Sáez, A., Lecampion, B., Bhattacharya, P., and Viesca, R. C. (2022). Three-dimensional fluid-driven stable frictional ruptures. *Journal of the Mechanics and Physics of Solids*, 160:104754.

[Sáez Uribe, 2023] Sáez Uribe, A. A. (2023). *Three-dimensional fluid-driven frictional ruptures: theory and applications*. PhD thesis, EPFL, Lausanne.

[Villiger et al., 2021] Villiger, L., Gischig, V., Kwiatek, G., Krietsch, H., Doetsch, J., Jalali, M., Amann, F., Giardini, D., and Wiemer, S. (2021). Meter-scale stress heterogeneities and stress redistribution drive complex fracture slip and fracture growth during a hydraulic stimulation experiment. *Geophysical Journal International*, 225.

[Xing et al., 2022] Xing, P., Damjanac, B., Moore, J., and McLennan, J. (2022). Flowback Test Analyses at the Utah Frontier Observatory for Research in Geothermal Energy (FORGE) Site. *Rock Mechanics and Rock Engineering*, 55(5):3023–3040.

6 Annexes

6.1 Variation of viscosity of the crosslinked CMHPG fluid when exposed to high temperatures

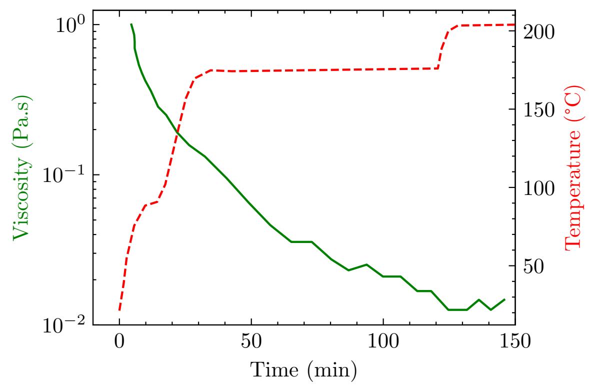

Figure 15: Variation of viscosity of the crosslinked CMHPG fluid used in the April 2022 stage 3 stimulation with time when exposed to high temperatures

6.2 Estimation of the aseismic rupture surface from the induced seismicity

We give here a more in-depth explanation of how we estimated the aseismic rupture area from the induced seismicity located events for the two hydraulic stimulation stages. As shown in Figure 6 and in Table 1, a lot more seismic events have been recorded for stage 3, which uses a more viscous fluid, than for stage 2, which uses a less viscous fluid, and the events seem to be well-aligned on a plane while the point cloud indicates a more complex rupture surface geometry for stage 2. For these reasons, to estimate the rupture area, we have projected the events on a single plane (the mean seismicity plane) for stage 3 while we have used several planes for stage 2. These planes come from a plane fitting exercise performed on the same seismic data by [Aleta et al., 2023]. These planes are shown in Figure 16.

To illustrate the following procedure of projecting the events on planes before computing convex hulls at various times, figure 17 shows what this looks like for stage 3. We can see what the induced seismicity looks like once projected on the mean seismicity plane and some examples of convex hulls at various time steps are represented. For the second stage, the procedure is identical except that we use several planes: we project the events on their closest plane and compute convex hulls on each plane at each time step. The aseismic rupture area is taken as the sum of the areas of the convex hulls. Finally, for the later stage, we have made the choice to filter some events considered as outliers in order to get a reasonable fracture surface estimation. Without doing so a few isolated events could contribute greatly to our estimation of the aseismic surface rupture, see Figure 8. More work could be done to come to a better criterion for outliers selection based on the space and time continuity of the events point cloud.

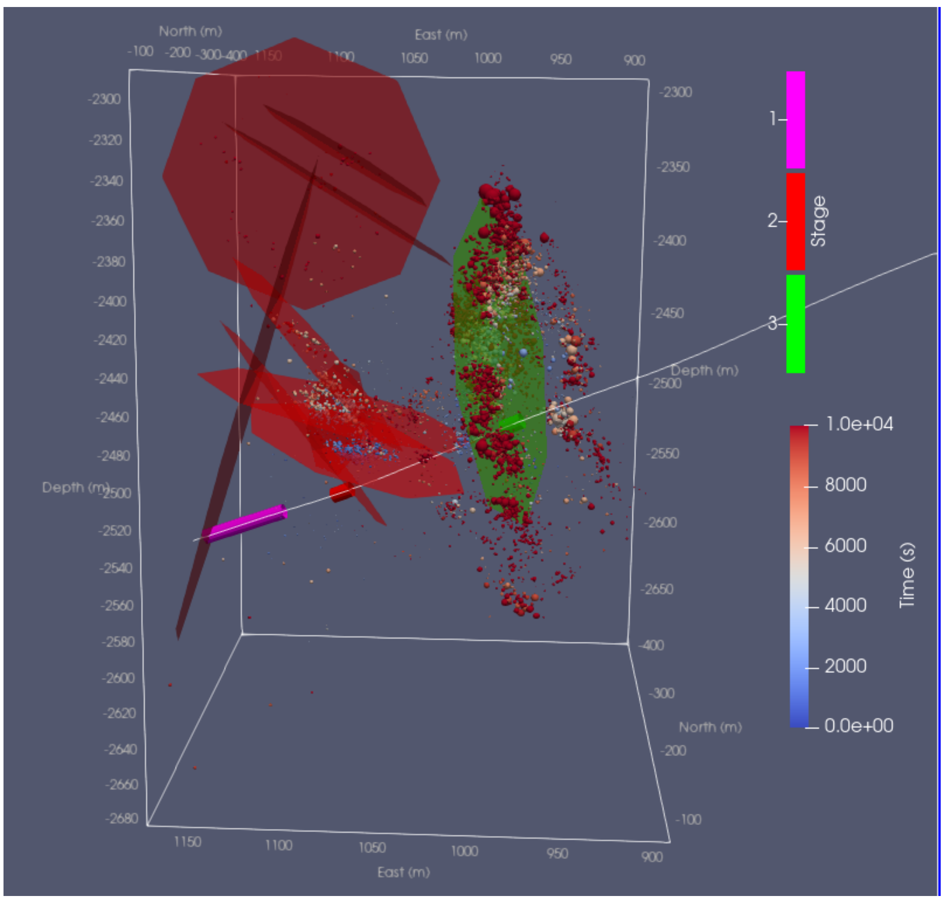

Figure 16: Planes used for the aseismic rupture surface estimation from the induced seismicity

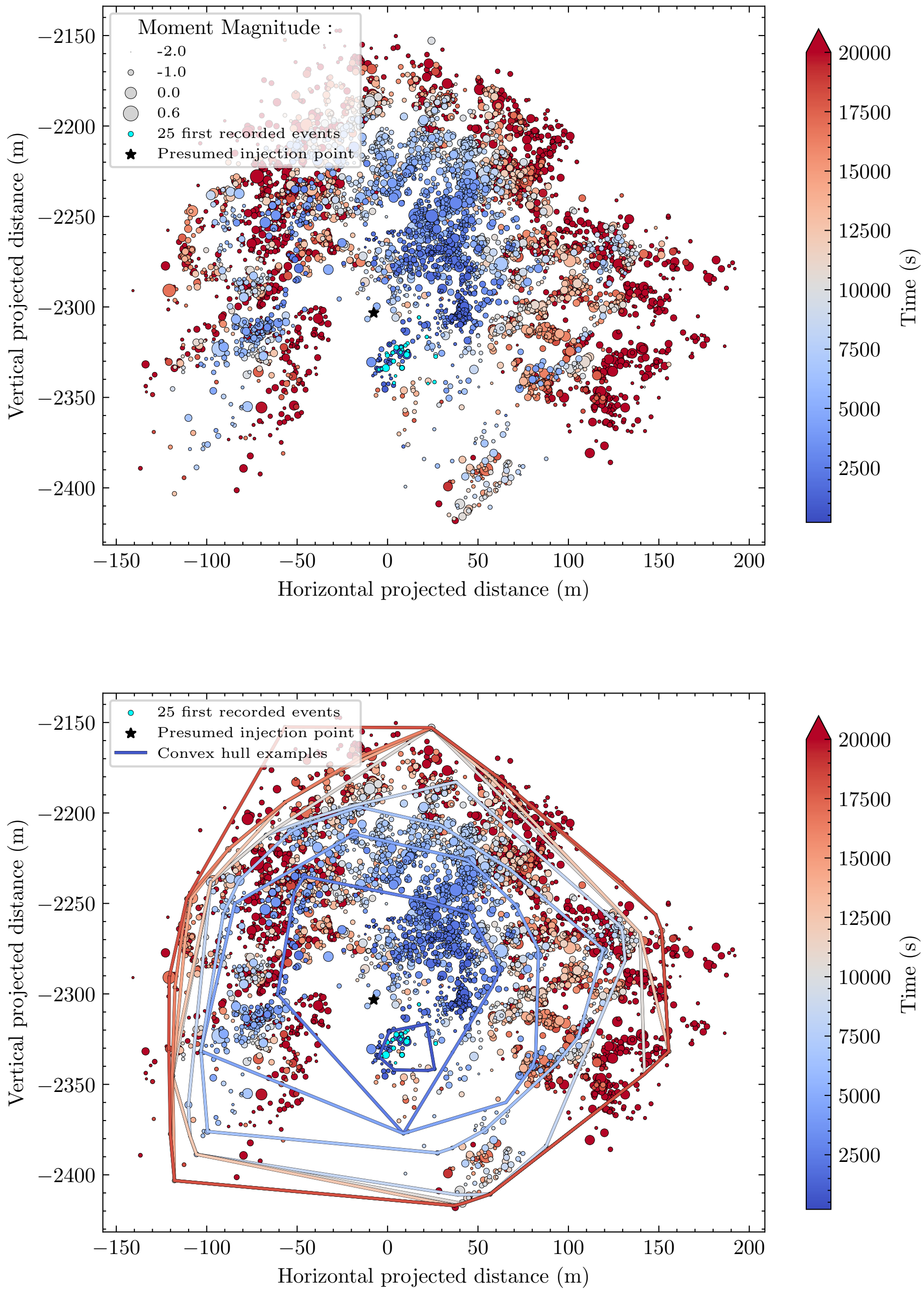

Figure 17: Stage 3 (viscous fluid) : projection of the induced seismicity on the mean seismicity plane and computation of convex hulls on these projected events at various times to estimate the aseismic rupture area.